

See discussions, stats, and author profiles for this publication at: <https://www.researchgate.net/publication/281102253>

# Biomimetic Nanoporous Anodic Alumina Distributed Bragg Reflectors in The Form of Films and Micro-Sized Particles for Sensing Applications

ARTICLE in ACS APPLIED MATERIALS & INTERFACES · AUGUST 2015

Impact Factor: 6.72 · DOI: 10.1021/acsaami.5b05904

---

READS

99

## 7 AUTHORS, INCLUDING:



Abel Santos

University of Adelaide

95 PUBLICATIONS 585 CITATIONS

[SEE PROFILE](#)



Ye Wang

University of Adelaide

17 PUBLICATIONS 76 CITATIONS

[SEE PROFILE](#)



Tushar Kumeria

University of California, San Diego

50 PUBLICATIONS 497 CITATIONS

[SEE PROFILE](#)



Dusan Losic

University of Adelaide

242 PUBLICATIONS 4,778 CITATIONS

[SEE PROFILE](#)

# Biomimetic Nanoporous Anodic Alumina Distributed Bragg Reflectors in the Form of Films and Microsized Particles for Sensing Applications

Yuting Chen,<sup>†,‡,§</sup> Abel Santos,<sup>\*,†</sup> Ye Wang,<sup>†</sup> Tushar Kumeria,<sup>†</sup> Junsheng Li,<sup>‡</sup> Changhai Wang,<sup>\*,§</sup> and Dusan Lasic<sup>†</sup>

<sup>†</sup>School of Chemical Engineering, The University of Adelaide, Engineering North Building, 5005 Adelaide, Australia

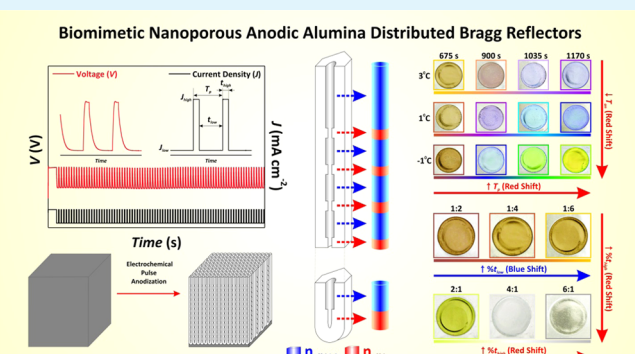
<sup>‡</sup>College of Food Science and Technology and <sup>§</sup>Jiangsu Key Laboratory of Marine Biology, College of Resources and Environmental Science, Nanjing Agricultural University, 210095 Nanjing, PR China

## Supporting Information

**ABSTRACT:** In this study, we produce for the first time biomimetic films and microsized particles based on nanoporous anodic alumina distributed Bragg reflectors (NAA-DBRs) by a rational galvanostatic pulse-anodization approach. These biomimetic photonic structures can feature a broad range of vivid bright colors, which can be tuned across the UV–visible spectrum by engineering their nanoporous structure through different anodization parameters. The effective medium of NAA-DBRs films is systematically assessed as a function of the anodization period, the anodization temperature, and the current density ratio by reflectometric interference spectroscopy (RIFS). This analysis makes it possible to establish the most sensitive structure toward changes in its effective medium.

Subsequently, specific detection of vitamin C molecules is demonstrated. The obtained results reveal that NAA-DBRs with optimized structure can achieve a low limit of detection for vitamin C molecules as low as 20 nM, a sensitivity of  $227 \pm 4 \text{ nm } \mu\text{M}^{-1}$ , and a linearity of 0.9985. Finally, as proof of concept, we developed a new photonic nanomaterial based on NAA-DBR microsized particles, which could provide new opportunities to produce microsized photonic analytical tools.

**KEYWORDS:** pulse anodization, structural engineering, nanoporous anodic alumina, biomimetic photonic coatings, reflectometric interference spectroscopy



## 1. INTRODUCTION

Many living organisms such as butterflies, beetles, and birds have evolved to modify, optimize, and adapt their visual appearance through structurally colored coatings. In these smart photonic coatings, which do not incorporate any natural pigment, color is generated by the interaction between light and matter. Colored films can be naturally or synthetically created by a range of photonic nanostructures, including diffraction gratings, selective mirrors, photonic crystals, crystal fibers, or matrices of nanopores. Nanomaterials such as thin films can be produced with a broad range of colors by means of different synthetic approaches.<sup>1–4</sup> Although the color of a material is not relevant for many applications, this optical property can be a key factor in order to spread its applicability toward other uses. An outstanding example of that is porous silicon (pSi), which can be produced with a broad range of vivid colors by engineering its nanoporous structure.<sup>5–7</sup> This physical property has spread the use of pSi nanostructures in the form of films and microparticles to a plethora of new applications, including optical/visual sensing, optoelectronics, drug delivery, cosmetics, protective films, food technology, and so on.<sup>8–13</sup> It is worth noting that pSi oxidizes in air

or aqueous solutions and degrades under acidic or basic media conditions unless passivated via chemical functionalization or carbonization.<sup>14–16</sup> Oxidation and degradation of pSi lead to unstable optical signals and changes in color. This property, which can be readily useful in some applications such as drug delivery nanocarriers and in vivo visual sensors, can prevent pSi from being used in those applications where a stable color is desired.<sup>17–20</sup>

Alternative inert and chemically passive nanoporous materials such as nanoporous anodic alumina (NAA) could overcome these limitations. NAA is produced by electrochemical anodization of aluminum substrates in acid electrolytes, and its nanopores can be structurally engineered by means of different electrochemical approaches such as pulse anodization.<sup>21–27</sup> Recently, some studies have made good use of these fabrication methods to produce a variety of photonic structures based on NAA such as rugate filters and distributed Bragg reflectors

Received: July 1, 2015

Accepted: August 19, 2015

Published: August 19, 2015

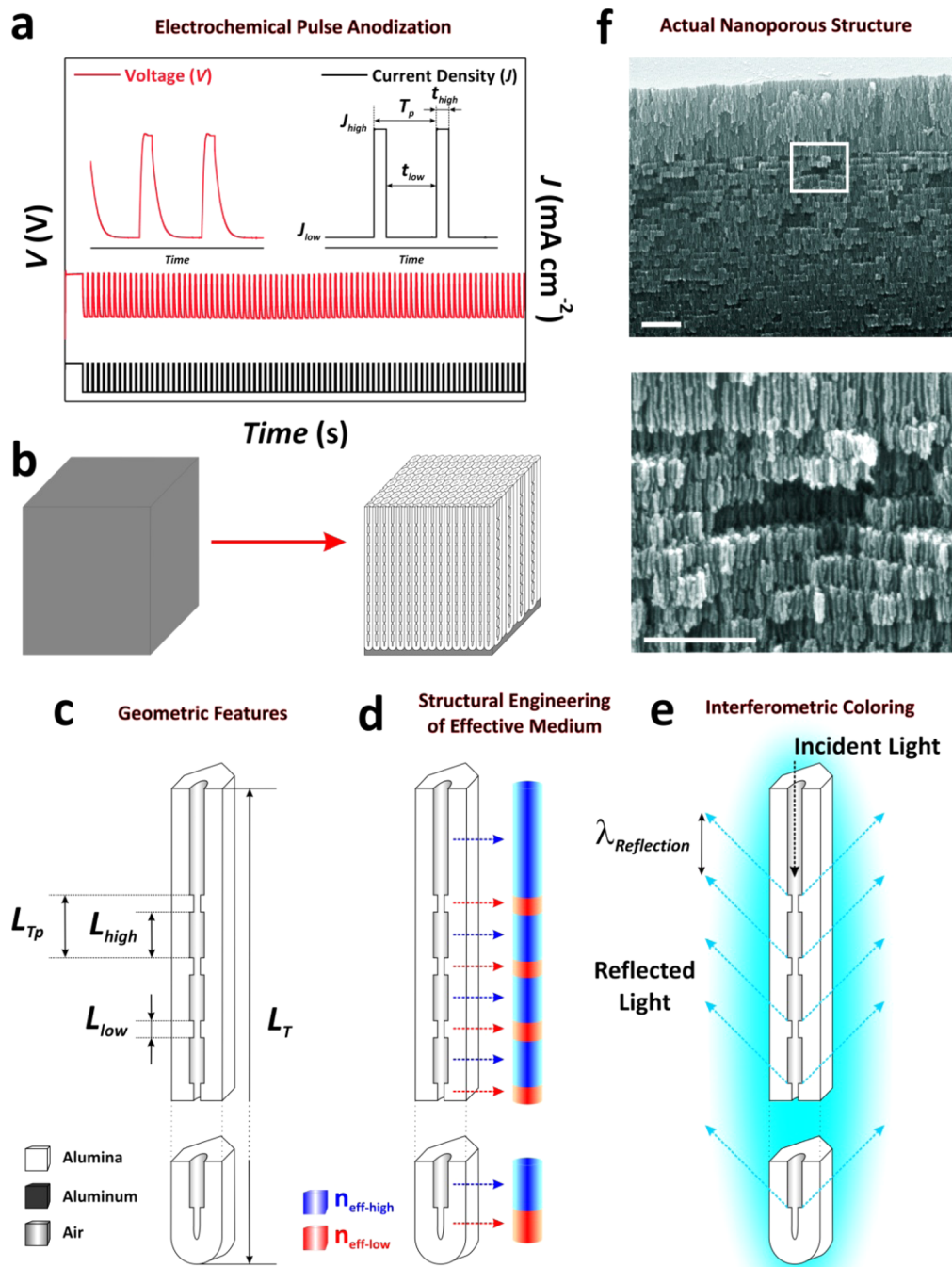


**Figure 1.** Fabrication of photonic films based on NAA-DBRs. (a) Example of pulse anodization profile describing the different parameters defining a current density pulse (i.e.,  $T_p$ ,  $J_{high}$ ,  $J_{low}$ ,  $t_{high}$ , and  $t_{low}$ ). (b) Scheme describing the fabrication of NAA-DBRs. (c) Illustration defining the different geometric features in NAA-DBRs (i.e.,  $L_T$ ,  $L_{Tp}$ ,  $L_{high}$ , and  $L_{low}$ ). (d) Illustration depicting how the effective medium is structurally engineered in depth in NAA-DBRs ( $n_{eff-high} < n_{eff-low}$ ). (e) Scheme illustrating how NAA-DBRs reflect light at specific wavelengths by the interaction light–matter (i.e., generation of interferometric colors). (f) Representative SEM images showing the actual nanoporous structure of NAA-DBRs (top, general cross-sectional view; bottom, magnified view of white square shown in top. Scale bars = 1  $\mu$ m and 500 nm, respectively).

(DBRs).<sup>28–36</sup> NAA is a very attractive material in terms of chemical and physical properties (e.g., controllable nanopore geometry, chemical stability, mechanical robustness, easy chemical functionalization, etc.). Furthermore, the optical signals and sensing performance of NAA-based photonic structures are comparable to those of porous silicon.<sup>37,38</sup> Nevertheless, NAA photonic structures feature transparent color unless the remaining aluminum substrate is chemically removed because of

its intrinsic photonic limitations (i.e., low contrast of porosity between nanoporous layers and low refractive index, approximately  $n_{NAA} = 1.67$ ). These inherent limitations, however, can be overcome by modifying the anodization conditions so that the resulting NAA layers feature high porosity and thus high contrast of effective refractive index between layers.<sup>39</sup> Under specific anodization conditions, NAA can be produced with vivid colors, which can be tuned across the UV–visible spectrum by structural

**Table 1.** Fabrication Parameters (i.e.,  $T_p$ ,  $T_{an}$ , and  $R_t$ ) for the Different NAA-DBR Photonic Films Produced in This Study, the Spectrum Range Where These Photonic Structures Reflect Light, and the RGB Color of the Resulting Film<sup>a</sup>

Label	$T_p$ (s)	$T_{an}$ (°C)	$R_t$	Range	RGB
NAA-DBR <sub>(675s;3°C;1:4)</sub>	675	3	1:4	UV	(205,186,102)
NAA-DBR <sub>(900s;3°C;1:4)</sub>	900	3	1:4	UV	(191,171,156)
NAA-DBR <sub>(1035s;3°C;1:4)</sub>	1035	3	1:4	Visible	(209,212,233)
NAA-DBR <sub>(1170s;3°C;1:4)</sub>	1170	3	1:4	Visible	(199,206,228)
NAA-DBR <sub>(675s;1°C;1:4)</sub>	675	1	1:4	UV	(207,193,119)
NAA-DBR <sub>(900s;1°C;1:4)</sub>	900	1	1:4	Visible	(187,177,225)
NAA-DBR <sub>(1035s;1°C;1:4)</sub>	1035	1	1:4	Visible	(185,230,232)
NAA-DBR <sub>(1170s;1°C;1:4)</sub>	1170	1	1:4	Visible	(164,199,228)
NAA-DBR <sub>(675s;-1°C;1:4)</sub>	675	-1	1:4	UV	(186,158,70)
NAA-DBR <sub>(900s;-1°C;1:4)</sub>	900	-1	1:4	Visible	(187,221,220)
NAA-DBR <sub>(1035s;-1°C;1:4)</sub>	1035	-1	1:4	Visible	(197,253,106)
NAA-DBR <sub>(1170s;-1°C;1:4)</sub>	1170	-1	1:4	Visible	(225,229,40)
NAA-DBR <sub>(675s;3°C;1:2)</sub>	675	3	1:2	UV	(225,229,40)
NAA-DBR <sub>(675s;3°C;1:6)</sub>	675	3	1:6	UV	(194,168,58)
NAA-DBR <sub>(675s;3°C;2:1)</sub>	675	3	2:1	Visible	(192,199,51)
NAA-DBR <sub>(675s;3°C;4:1)</sub>	675	3	4:1	Visible	(223,224,217)
NAA-DBR <sub>(675s;3°C;6:1)</sub>	675	3	6:1	Visible	(190,194,164)

<sup>a</sup>RGB values shown in Table 1 are only for comparison among samples.

engineering. These photonic structures can efficiently reflect light at specific wavelengths across the UV–visible spectrum, enabling the production of interferometrically colored aluminum (Figure 1).

Herein, we present a systematic study on the fabrication, engineering, optical assessment, and sensing applicability of NAA-DBR photonic films. This study demonstrates the outstanding potential of NAA-DBR photonic films as optical sensing platforms in the form of films and nanoporous microparticles.

## 2. EXPERIMENTAL SECTION

**2.1. Materials.** High-purity (99.9997%) aluminum foils, 0.32 mm thick, were supplied by Goodfellow Cambridge, Ltd. (UK). Sulfuric acid ( $H_2SO_4$ ), perchloric acid ( $HClO_4$ ), chromium trioxide ( $CrO_3$ ), phosphoric acid ( $H_3PO_4$ ), hydrochloric acid (HCl), cupric chloride ( $CuCl_2$ ), (3-aminopropyl)trimethoxysilane (APTES), hydrogen peroxide ( $H_2O_2$ ), L-ascorbic acid ( $C_6H_8O_6$ , vitamin C), and glutaraldehyde ( $CH_2(CH_2CHO)_2$ , GTA) were purchased from Sigma-Aldrich (Australia). Ethanol ( $C_2H_5OH$  – EtOH) and isopropanol ( $C_3H_8O$  – IPA) were supplied by ChemSupply (Australia). Ultrapure water from Option Q-Purelabs (Australia) was used for preparing the aqueous solutions used in this study.

**2.2. Fabrication of NAA-DBRs.** NAA-DBR structures were produced by galvanostatic pulse anodization in an aqueous solution of 1.1 M  $H_2SO_4$ . Al substrates were first electropolished in a mixture of EtOH and  $HClO_4$  (4:1 (v/v)) at 20 V and 5 °C for 3 min prior to anodization in order to achieve a mirrorlike finish. After that, Al substrates were first anodized in 1.1 M  $H_2SO_4$  for 1 h at a constant current density of 1.12 mA cm<sup>-2</sup>. Next, the anodization profile was set to pulse mode, during which the current density was sequentially pulsed in a stepwise fashion between high ( $J_{high} = 1.12$  mA cm<sup>-2</sup>) and low ( $J_{low} = 0.28$  mA cm<sup>-2</sup>) current density values for a total of 150 pulses. In the case of NAA-DBRs fabricated at -1 °C, the acid electrolyte solution was modified with 25 vol % of EtOH in order to prevent the solution from freezing.<sup>40–42</sup>

**2.3. Specific Detection of Vitamin C.** The most sensitive NAA-DBR structure was used to evaluate the ability of these photonic structures as optical sensing platform for specific detection of analytes. The inner surface of NAA-DBR photonic films was chemically modified with APTES by a well-established silanization process reported elsewhere.<sup>43</sup> In brief, the inner surface of NAA-DBRs was first hydroxylated in boiling  $H_2O_2$  (30 wt %) for 10 min. Then, NAA-DBRs were dried and functionalized with APTES via chemical vapor deposition at 135 °C for 3 h. The sensing performance of the most sensitive NAA-DBR structure under specific adsorption conditions was assessed by measuring changes

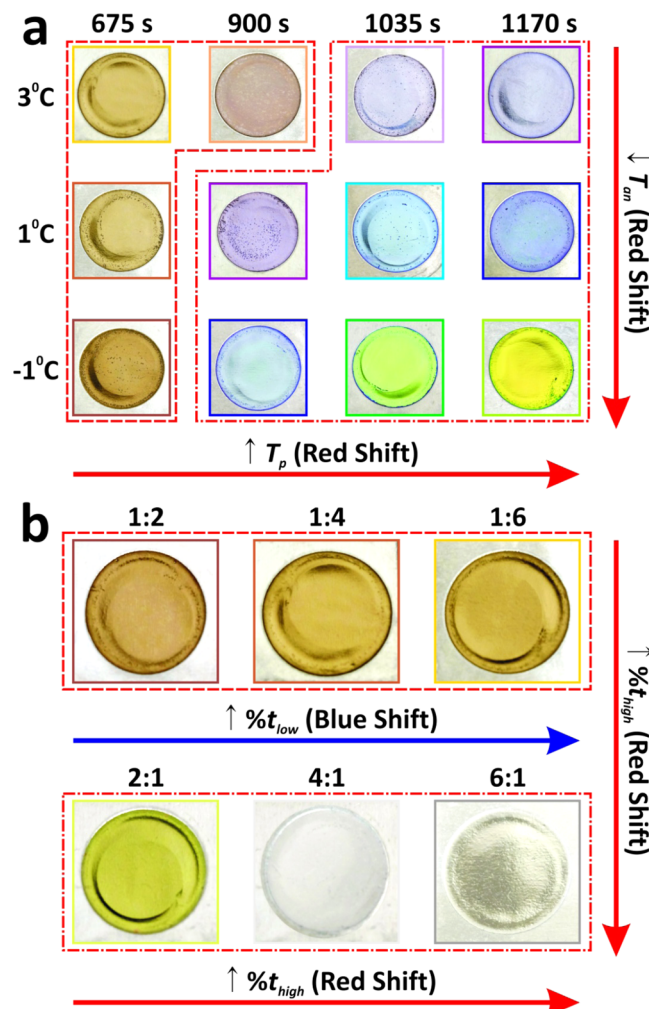


**Figure 2.** Digital pictures of NAA-DBR photonic films featuring different colors tuned by different fabrication parameters. Aluminum substrates were anodized through a circular window of 1 cm in diameter = diameter of NAA-DBR photonic films. Dashed line = UV range; dotted and dashed line = visible range. (a) Effect of  $T_p$  and  $T_{an}$ . (b) Effect of  $R_t$ .

in the effective optical thickness ( $OT_{eff}$ ) of these films with the concentration of vitamin C. To this end, five different analytical solutions of

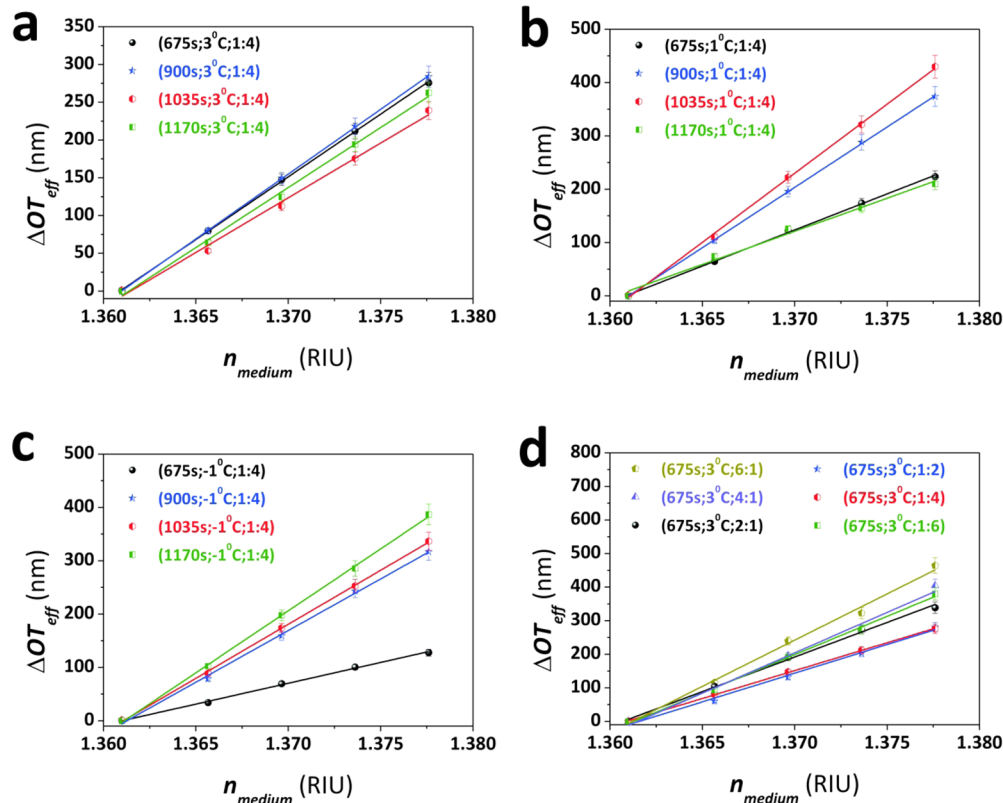


**Figure 3.** Assessment of effective medium of NAA-DBR photonic films by RIFS as a function of the fabrication parameters (i.e.,  $T_p$ ,  $T_{an}$ , and  $R_t$ ) and the effective refractive index of the medium filling the nanopores (i.e.,  $n_{medium}$ ). (a–c)  $\Delta OT_{eff}$  as a function of  $T_p$  at  $R_t = 1:4$  and  $T_{an} = 3$ , 1, and  $-1$  °C, respectively. (d)  $\Delta OT_{eff}$  as a function of  $R_t$  at  $T_p = 675$  s and  $T_{an} = 3$  °C.

vitamin C were used (i.e., 0.125, 0.188, 0.250, 0.375, and 0.500  $\mu$ M). This set of experiments was performed in a flow cell, where  $\Delta OT_{eff}$  of the NAA-DBR films was monitored in real-time at a flow rate of 100  $\mu$ L min<sup>-1</sup>. A stable baseline with ultrapure water was established for 15 min prior to injection of the different analytical solutions, and amine terminal groups of APTES molecules ( $-NH_2$ ) were activated by flowing an aqueous solution of GTA 2.5 vol % for 15 min. The contact of vitamin C molecules with GTA-APTES-functionalized NAA-DBR films produced sharp changes in the  $OT_{eff}$  of NAA-DBRs and continued until total saturation of the amine groups present on the inner surface of NAA-DBRs. Finally, water was flowed again in order to remove physisorbed vitamin C molecules and establish the total  $\Delta OT_{eff}$  associated with immobilized vitamin C molecules.

#### 2.4. Generation of NAA-DBR Nanoporous Microparticles.

Nanoporous microparticles were prepared from NAA-DBR films by selective chemical removal of the remaining aluminum substrates in a saturated mixture of HCl/CuCl<sub>2</sub>. After that, NAA-DBR films were broken down into microparticles first by mortar grinding and then by sonication during 2 h. The resulting NAA-DBR microparticles were characterized by optical microscopy (Nikon LV100 POL optical petrographic microscope).

**2.5. Morphological Characterization.** The morphological characteristics of the different types of NAA-DBR films were characterized by field-emission gun scanning electron microscopy (FEG-SEM FEI Quanta 450). The plugin Measure RGB in ImageJ (public domain program developed at the RSB of the NIH) was used for SEM image analysis and the plugin Measure RGB was used to establish the RGB values of each sample. RGB color scales were established by image analysis of digital pictures of NAA-DBRs acquired by a mobile phone Sony Xperia™ Z3 Compact equipped with a camera of 20.7 MP (5248 × 3936 pixels) and autofocus function.<sup>44</sup>

## 3. RESULTS AND DISCUSSION

### 3.1. Tuning Color in NAA-DBR by Structural Engineering of Nanopore Geometry.

NAA-DBRs were produced by pulse

anodization under mild conditions (Figure 1a). As Figure 1b depicts, the structure of NAA-DBR photonic films can be described as a stack of nanoporous strata featuring sequentially alternated levels of porosity in depth. The geometry of NAA-DBRs can be defined by the lengths of the segments with high and low effective refractive index ( $L_{high}$  and  $L_{low}$ , respectively), the period length ( $L_{Tp}$ , defined as  $L_{high} + L_{low}$ ), and the total thickness of the film ( $L_T$ ) (Figure 1c). Table S1 summarizes the values of pore diameter, growth rate, and porosity of NAA produced at  $J_{high}$  and  $J_{low}$  respectively. The light–matter interaction can be engineered by the nanoporous structure of NAA-DBRs, making it possible to tune color of NAA-DBRs across the UV–visible spectrum by switching the effective refractive index of NAA between high ( $n_{eff,low}$  i.e., low anodization current density) and low ( $n_{eff,high}$  i.e., high anodization current density) values (Figure 1d,e). Figure 1f shows a set of representative SEM images of the actual nanoporous structure of NAA-DBRs produced in this study.

To shed light on the different parameters affecting the generation of color in NAA-DBR structures and fabricate a complete library of NAA-DBR structures with colors across the UV–visible spectrum, the length of the current density pulse period ( $T_p$ ), the anodization temperature ( $T_{an}$ ), and the ratio of time for high and low current density values ( $R_t$ ) were set to four, three, and six different values, respectively (i.e.,  $T_p = 675$ , 900, 1035, and 1170 s;  $T_{an} = 3$ , 1, and  $-1$  °C;  $R_t = 1:2$ , 1:4, 1:6, 2:1, 4:1, and 6:1). Note that  $T_p$  is defined as the total time length of high and low anodization current density pulses (eq 1), and  $R_t$  is defined as the ratio between the time duration of high ( $J_{high}$ ) and low ( $J_{low}$ ) anodization current density pulses, respectively (i.e.,  $t_{high}$  and  $t_{low}$ ) (eq 2).

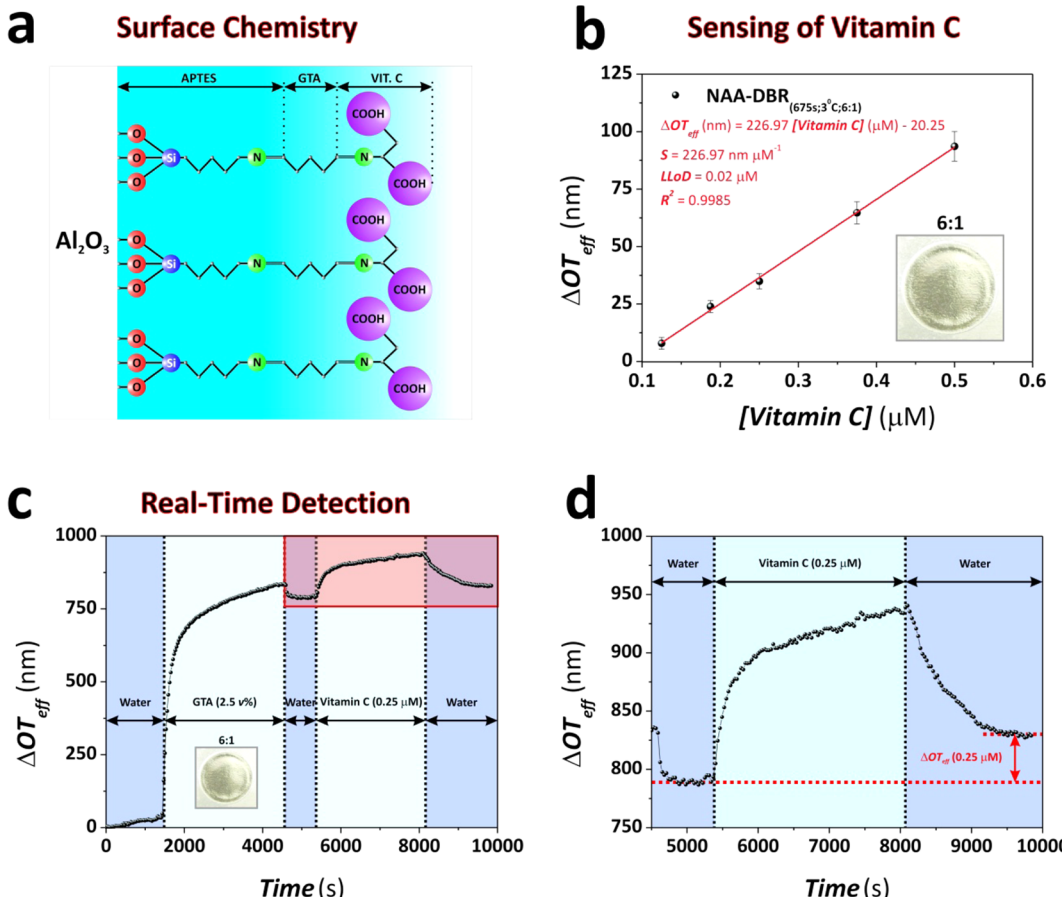


**Figure 4.** Selective detection of vitamin C molecules by NAA-DBRs combined with RIFs. (a) Illustration depicting the surface chemistry used to endow NAA-DBR films with chemical selectivity toward vitamin C molecules. (b) Sensing performance of NAA-DBR<sub>(675s;3°C;6:1)</sub> when detecting vitamin C molecules. (c) Example of real-time detection of vitamin C (0.25 μM) using ΔOT<sub>eff</sub> as sensing principle. (d) Magnified view of red rectangle shown in c.

$$T_p = t_{\text{high}} + t_{\text{low}} \quad (1)$$

$$R_t = t_{\text{high}} / t_{\text{low}} \quad (2)$$

The fabrication characteristics of the different NAA-DBR structures, the spectrum range where these photonic structures reflect light, and the RGB color values of the resulting films are summarized in Table 1; a description of the different parameters used to create the different anodization profiles used in this study is presented in Figure 1a (i.e.,  $T_p$ ,  $J_{\text{high}}$ ,  $J_{\text{low}}$ ,  $t_{\text{high}}$ , and  $t_{\text{low}}$ ).

Figure 2 shows digital pictures of the different NAA-DBRs. As these images reveal, light reflected by NAA-DBRs is shifted toward longer wavelengths (i.e., red-shifted) when the anodization period is increased (i.e., the longer  $T_p$ , the longer the wavelength of the reflected light). Representative reflection spectra shown in Figure S1 demonstrate that the maximum of the reflection spectrum in NAA-DBRs can be readily tuned across the UV-visible spectrum by the anodization period. Furthermore, our results demonstrate that this redshift can be further increased by decreasing the anodization temperature ( $T_{\text{an}}$ ). NAA-DBR structures can be produced with bright colors across the UV-visible spectrum, including brown, gold, pink, purple, blue, green, and yellow (Figure 2a). Further colors, including gold, white, and silver, can be produced by modifying the ratio between the time duration of high and low anodization current density pulses ( $R_t$ , Figure 2b).

Color in NAA-DBRs is created by light interference, a physical phenomenon that takes place when light falls on NAA-DBRs

from their top surface and interacts with their nanoporous structure. The wavelength at which that interference is constructive in a given NAA-DBR structure is established by the Bragg's law, adapted to NAA-DBRs, represented as eq 3:<sup>45</sup>

$$m\lambda = 2(L_{\text{high}}\sqrt{n_{\text{eff-high}}^2 - \sin \theta} + L_{\text{low}}\sqrt{n_{\text{eff-low}}^2 - \sin \theta}) \quad (3)$$

where  $m$  is the diffraction order, the maximum of which is located at the wavelength  $\lambda$ ,  $L_{\text{high}}$  and  $L_{\text{low}}$  are the lengths of the segments in the structure of the NAA-DBR with a high and low effective refractive index, respectively, and  $\theta$  is the transmitted beam angle within the film. That expression can be simplified if light is shined at normal incidence (i.e.,  $\theta = 0^\circ$ ):

$$m\lambda = 2(L_{\text{high}}n_{\text{eff-high}} + L_{\text{low}}n_{\text{eff-low}}) \quad (4)$$

Therefore, according to the Bragg's law, NAA-DBR photonic films reflect light at longer wavelengths when  $T_p$  is increased because  $L_{T_p}$  is directly proportional to  $L_{\text{high}}$  and  $L_{\text{low}}$  (i.e.,  $\uparrow T_p \rightarrow \uparrow L_{T_p} \rightarrow \uparrow(L_{\text{high}} + L_{\text{low}}) \rightarrow \uparrow\lambda$ ) (Figure 2a). Furthermore, that redshift can be further increased for a given  $T_p$  by decreasing the anodization temperature because the porosity level of each layer is decreased ( $\downarrow T_{\text{an}} \rightarrow \uparrow(n_{\text{eff-high}} + n_{\text{eff-low}}) \rightarrow \uparrow\lambda$ ; Figure 2a).<sup>21</sup> As mentioned before,  $R_t$  is defined as the ratio  $t_{\text{high}}/t_{\text{low}}$  (eq 2). The growth rate of layers at high current density ( $J_{\text{high}}$ ) is much faster than that of layers produced at low current density ( $J_{\text{low}}$ ) (Table S1).<sup>21</sup> Therefore, when the proportion of  $t_{\text{high}}$  in  $R_t$  is

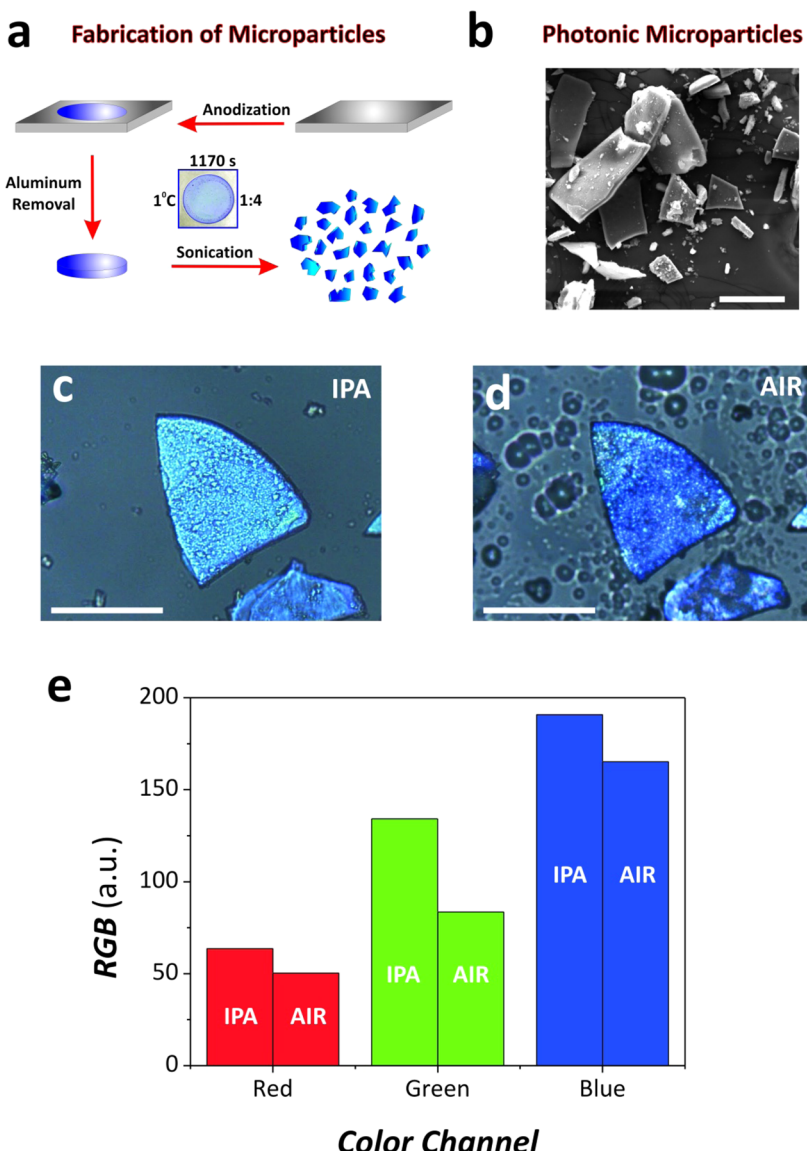


**Figure 5.** Concept of sensing application of microsized nanoporous photonic particles derived from NAA-DBR films. (a) Illustration of the fabrication process used to produce microsized NAA-DBR particles from NAA-DBR<sub>(1170 s; 3°C; 1:4)</sub>. (b) Representative SEM image of microsized particles (scale bar = 50  $\mu$ m). (c and d) Optical images of microsized NAA-DBR particles in isopropanol (IPA) and air (scale bar = 50  $\mu$ m). (e) Decomposition of colors in RGB values for images shown in c and d.

increased, the wavelength of the reflected light is shifted toward longer wavelengths according to eq 4 (Figure 2b).

**3.2. Evaluation of Optical Characteristics of NAA-DBRs by RIfS.** NAA-DBRs are a composite material based on stacked layers of NAA featuring different levels of porosity. The optical properties of this material can be described by the effective medium approximation, in which the macroscopic properties of composite materials result from averaging the properties of individual constituents.<sup>46</sup> Reflectometric interference spectroscopy (RIfS) was the technique of choice used to assess the sensitivity ( $S$ ), low limit of detection (LLoD), and linearity ( $R^2$ ) of the effective medium of the different NAA-DBRs.<sup>47–52</sup> To this end, the nanoporous network of NAA-DBRs was infiltrated with four different mixtures of ethanol (EtOH) and isopropanol (IPA) (i.e., EtOH/IPA (v/v) = 3:1, 1:1, 1:3, and 0:1) in order to achieve a broad contrast of refractive index of the medium filling the nanopores ( $n_{\text{medium}}$  = 1.366, 1.370, 1.374, and 1.378 RIU, respectively). Note that the total effective optical thickness

change was calculated as the difference between the corresponding effective optical thickness and the effective optical thickness of the film when infiltrated with ethanol (i.e., baseline  $n_{\text{EtOH}} = 1.361$  RIU). The above-mentioned optical characteristics were evaluated by measuring the changes in the effective optical thickness of NAA-DBRs ( $\Delta OT_{\text{eff}}$ ) at normal incidence after infiltration with media of different refractive indexes (eq 5).

$$\Delta OT_{\text{eff}} = 2n_{\text{eff}}L_T \quad (5)$$

where  $OT_{\text{eff}}$  is the effective optical thickness of the film,  $n_{\text{eff}}$  is its effective refractive index, and  $L_T$  is its physical thickness.

Note that  $\Delta OT_{\text{eff}}$  was monitored in real-time using a flow cell combined with a RIfS system. (See details in Figure S2.) The obtained results, which are summarized in Figure 3a–d and Table S2, reveal that the most sensitive structure was NAA-DBR<sub>(675 s; 3°C; 6:1)</sub>, with a sensitivity of  $27\text{ SS}3 \pm 1148\text{ nm RIU}^{-1}$ . In terms of LLoD and linearity, the most optimal NAA-DBR

structure was NAA-DBR<sub>(900s;3°C;1:4)</sub>, with LLoD of 0.028 RIU and  $R^2$  of 0.9999.

Motivated by these results, we decided to assess the sensing performance of the most sensitive photonic nanostructure (i.e., NAA-DBR<sub>(675s;3°C;6:1)</sub>) when detecting vitamin C in a chemically selective manner.

**3.3. NAA-DBRs as Optical-Sensing Platform for Detection of Vitamin C.** A set of NAA-DBR structures (i.e., type NAA-DBR<sub>(675s;3°C;6:1)</sub>) was chemically modified with (3-aminopropyl)-trimethoxysilane (APTES) in order to achieve chemical specificity toward vitamin C molecules (Figure 4a). Figure S3 shows a representative RIFS spectrum of this type of NAA-DBR structure. A total of five analyte solutions of vitamin C (i.e., 0.125, 0.188, 0.250, 0.375, and 0.500  $\mu\text{M}$ ) was used to characterize the sensing performance of NAA-DBRs. Figure 4b summarizes the obtained results, which reveal that NAA-DBRs can provide a sensitivity of  $227 \pm 4 \text{ nm } \mu\text{M}^{-1}$ , a LLoD of 20 nM, and a linearity of 0.9985 for vitamin C molecules. Figure 4c,d shows an example of real-time sensing of vitamin C for a concentration of 0.25  $\mu\text{M}$ . These outstanding sensing capabilities are unprecedented for a system of its class and demonstrate that a rational design of the structure of NAA-DBR photonic films makes it possible to detect trace levels of analytes.

**3.4. Nanoporous Microparticles from NAA-DBRs.** Finally, as a proof of concept, we demonstrated that NAA-DBR photonic films keep their optical properties when they are fractured into microsized nanoporous particles. NAA-DBRs undergo sharp changes in color when their nanoporous structure is filled with different media. This optical property can be readily used to develop visual sensing systems based on color changes. Each of these microparticles contains the same spectroscopic identity and chemical sensing capabilities as those of the original NAA-DBR photonic film, making it possible to produce individual microsized optical sensors. Figure 5a depicts the fabrication process of this new photonic nanomaterial, which was produced by selective removal of the remaining aluminum substrate and subsequent fracture of the NAA-DBR photonic film by sonication. As Figure 5b shows, microparticles based on NAA-DBRs with an average size of  $45 \pm 8 \mu\text{m}$  feature the same vivid color as the original film. Figure 5c,d shows how microsized nanoporous particles undergo color changes when they are infiltrated by different media (i.e., isopropanol (IPA) and air; Supporting Information Video). Furthermore, this property can be readily used to implement microsized sensors based on colorimetry. Figure 5e shows the decomposition in RGB values of the digital pictures of microsized NAA-DBRs shown in Figure 5c,d. This analysis demonstrates that these photonic microparticles can be used for quantification of analytes through color changes, opening new opportunities to spread the applicability of NAA toward other uses such as microsensors, self-reporting nanocarriers, tags, tracers, and so on.

## CONCLUSIONS

This study has reported on a rational approach aimed to develop photonic films based on NAA-DBRs. These photonic nanostructures feature vivid colors across the UV-visible spectrum, which can be precisely tuned by engineering the nanoporous structure of these photonic films in a systematic manner. A total of 18 NAA-DBR photonic films were produced, and their effective medium systematically was assessed by reflectometric interference spectroscopy. The obtained results reveal that the nanostructure with the most sensitive effective medium was NAA-DBR<sub>(675s;3°C;6:1)</sub>, which was produced with an anodization

period of 675 s and a current ratio of 6:1 at an anodization temperature of 3 °C. This type of NAA-DBR photonic film was then evaluated as sensing platforms to detect vitamin C molecules. The obtained results demonstrate that this type of NAA-DBRs presents unprecedented sensing capabilities, with a sensitivity of  $227 \pm 4 \text{ nm } \mu\text{M}^{-1}$ , a LLoD of 20 nM, and a linearity of 0.9985. Finally, as proof of concept, we developed a new photonic nanomaterial based on NAA-DBR microsized particles, which opens new opportunities for producing innovative analytical tools in the near future.

## ASSOCIATED CONTENT

### S Supporting Information

The Supporting Information is available free of charge on the ACS Publications website at DOI: 10.1021/acsami.5b05904.

Further information about values of pore growth rate and porosity of NAA produced at  $J_{\text{high}}$  and  $J_{\text{low}}$ , examples of reflection spectra showing how the position of the maximum reflection peak can be tuned by the anodization period, real-time monitoring of  $\Delta OT_{\text{eff}}$  when the nanopores are infiltrated with different mixtures of ethanol and isopropanol, and a summary table with the sensitivity, low limit of detection, and linearity values of the whole set of NAA-DBRs assessed in this study. (PDF)

A supporting video file is included, demonstrating the potential applicability of microsized nanoporous particles based on NAA-DBRs for visual detection of analytes. (AVI).

## AUTHOR INFORMATION

### Corresponding Authors

\*Phone: +61 8 8313 1535. Fax: +61 8 8303 4373. E-mail: abel.santos@adelaide.edu.au. Web: <http://www.adelaide.edu.au/directory/abel.santos>.

\*Phone: +86 025 84396680. Fax: +86 025 84396680. E-mail: chwang@njau.edu.cn. Web: <http://re.njau.edu.cn/html/szll/hyswxx/yjs/2014/09/28/f3c70e8c-facd-482b-b186-8dc68ec757c4.html>.

### Author Contributions

A.S. designed the experimental part of this work. Y.C. carried out the experiments assisted by A.S.

### Notes

The authors declare no competing financial interest.

## ACKNOWLEDGMENTS

We are thankful for the support provided by the Australian Research Council (ARC) through grant nos. DE140100549, DP120101680, and FT110100711 and the School of Chemical Engineering (UoA). Authors thank the Adelaide Microscopy (AM) center for FEG-SEM characterization. We also are thankful for the support from Nanjing Agricultural College dominant disciplines Innovation Fund 080-80900211-52, Natural Science Foundation of Jiangsu Province (BK20140713) and National High Technology Research and Development Program of China (2012AA021706).

## ABBREVIATIONS

NAA-DBRs, nanoporous anodic alumina distributed Bragg reflectors

RIFS, reflectometric interference spectroscopy

S, sensitivity

LLoD, low limit of detection

## ■ REFERENCES

- (1) Li, J.; Liang, G.; Zhu, X.; Yang, S. Exploiting Nanoroughness on Holographically Patterned Three-Dimensional Photonic Crystals. *Adv. Funct. Mater.* **2012**, *22*, 2980–2986.
- (2) Ishizaki, T.; Sakamoto, M. Facile Formation of Biomimetic Color-Tuned Superhydrophobic Magnesium Alloy with Corrosion Resistance. *Langmuir* **2011**, *27*, 2375–2381.
- (3) Huang, Y. F.; Jen, Y. J.; Chen, L. C.; Chen, K. H.; Chattopadhyay, S. Design for Approaching Cicada-Wing Reflectance in Low- and High-Index Biomimetic Nanostructures. *ACS Nano* **2015**, *9*, 301–311.
- (4) Feng, L.; Zhang, Y.; Li, M.; Zheng, Y.; Shen, W.; Jiang, L. The Structural Color of Red Rose Petals and Their Duplicates. *Langmuir* **2010**, *26*, 14885–14888.
- (5) Canham, L. T. Color of Porous Silicon. In *Handbook of Porous Silicon*; Canham, L. T., Ed.; Springer International Publishing: Zug, Switzerland, 2014; pp 1–7.
- (6) Lazarouk, S.; Jaguirio, P.; Katsouba, S.; Maiello, G.; La Monica, S.; Masini, G.; Proverbio, E.; Ferrari, A. Visual Determination of Thickness and Porosity of Porous Silicon Layers. *Thin Solid Films* **1997**, *297*, 97–101.
- (7) Sailor, M. J. Color Me Sensitive: Amplification and Discrimination in Photonic Silicon Nanostructures. *ACS Nano* **2007**, *1*, 248–252.
- (8) Lin, V. S. Y.; Motesharei, K.; Dancil, K. S.; Sailor, M. J.; Ghadiri, M. R. A Porous Silicon-Based Optical Interferometric Biosensor. *Science* **1997**, *278*, 840–843.
- (9) Canham, L. T. The Silicon Chameleon. *Nature* **1993**, *365*, 695.
- (10) Anglin, E. J.; Cheng, L.; Freeman, W. R.; Sailor, M. J. Porous Silicon in Drug Delivery Devices and Materials. *Adv. Drug Delivery Rev.* **2008**, *60*, 1266–1277.
- (11) Canham, L. T. Porous Silicon for Oral Hygiene and Cosmetics. In *Handbook of Porous Silicon*; Canham, L. T., Ed.; Springer International Publishing: Zug, Switzerland, 2014; pp 999–1008.
- (12) Canham, L. T.; Aston, R. *Method of Protecting Skin from UV Radiation Using A Dermatological Composition Having Porous Silicon*, U.S. Patent 8128912B2, March 6, 2012.
- (13) Canham, L. T. Porous Silicon and Functional Foods. In *Handbook of Porous Silicon*; Canham, L. T., Ed.; Springer International Publishing: Zug, Switzerland, 2014; pp 985–997.
- (14) Ariza-Avidad, M.; Nieto, A.; Salinas-Castillo, A.; Capitan-Vallvey, L. F.; Miskelly, G. M.; Sailor, M. J. Monitoring of Degradation of Porous Silicon Photonic Crystals Using Digital Photography. *Nanoscale Res. Lett.* **2014**, *9*, 410.
- (15) Jalkanen, T.; Mäkilä, E.; Suzuki, Y. I.; Urata, T.; Fukami, K.; Sakka, T.; Salonen, J.; Ogata, Y. H. Studies on Chemical Modification of Porous Silicon-Based Graded-Index Optical Microcavities for Improved Stability Under Alkaline Conditions. *Adv. Funct. Mater.* **2012**, *22*, 3890–3898.
- (16) Ciampi, S.; Harper, J. B.; Gooding, J. J. Wet Chemical Routes to The Assembly of Organic Monolayers on Silicon Surfaces via The Formation of Si–C Bonds: Surface Preparation, Passivation and Functionalization. *Chem. Soc. Rev.* **2010**, *39*, 2158–2183.
- (17) Hou, H.; Nieto, A.; Ma, F.; Freeman, W. R.; Sailor, M. J.; Cheng, L. Tunable Sustained Intravitreal Drug Delivery System for Daunorubicin Using Oxidized Porous Silicon. *J. Controlled Release* **2014**, *178*, 46–54.
- (18) Cheng, L.; Anglin, E.; Cunin, F.; Kim, D.; Sailor, M. J.; Falkenstein, I.; Tammewar, A.; Freeman, W. R. Intravitreal Properties of Porous Silicon Photonic Crystals: A Potential Self-Reporting Intraocular Drug-Delivery Vehicle. *Br. J. Ophthalmol.* **2008**, *92*, 705–711.
- (19) Low, S. P.; Voelcker, N. H.; Canham, L. T.; Williams, K. A. The Biocompatibility of Porous Silicon in Tissues of The Eye. *Biomaterials* **2009**, *30*, 2873–2880.
- (20) Wu, E. C.; Andrew, J. S.; Cheng, L.; Freeman, W. R.; Pearson, L.; Sailor, M. J. Real-Time Monitoring of Sustained Drug Release Using The Optical Properties of Porous Silicon Photonic Crystal Particles. *Biomaterials* **2011**, *32*, 1957–1966.
- (21) Lee, W.; Park, S. J. Porous Anodic Aluminum Oxide: Anodization and Templated Synthesis of Functional Nanostructures. *Chem. Rev.* **2014**, *114*, 7487–7556.
- (22) Lee, W.; Kim, J. C. Highly Ordered Porous Alumina with Tailor-Made Pore Structures Fabricated by Pulse Anodization. *Nanotechnology* **2010**, *21*, 485304.
- (23) Lee, W.; Kim, J.-C.; Gösele, U. Spontaneous Current Oscillations during Hard Anodization of Aluminum under Potentiostatic Conditions. *Adv. Funct. Mater.* **2010**, *20*, 21–27.
- (24) Masuda, H.; Fukuda, K. Ordered Metal Nanohole Arrays Made by a Two-Step Replication of Honeycomb Structures of Anodic Alumina. *Science* **1995**, *268*, 1466–1468.
- (25) Masuda, H.; Hasegawa, F. J. Self-Ordering of Cell Arrangement of Anodic Porous Alumina Formed in Sulfuric Acid Solution. *J. Electrochem. Soc.* **1997**, *144*, L127–L130.
- (26) Masuda, H.; Yada, K.; Osaka, A. Self-Ordering of Cell Configuration of Anodic Porous Alumina with Large-Size Pores in Phosphoric Acid Solution. *Jpn. J. Appl. Phys.* **1998**, *37*, L1340–L1342.
- (27) Nielsch, K.; Choi, J.; Schwirn, K.; Wehrspohn, R. B.; Gösele, U. Self-ordering Regimes of Porous Alumina: The 10% Porosity Rule. *Nano Lett.* **2002**, *2*, 677–680.
- (28) Santos, A.; Kumeria, T.; Losic, D. Optically Optimized Photoluminescent and Interferometric Biosensors Based on Nanoporous Anodic Alumina: A Comparison. *Anal. Chem.* **2013**, *85*, 7904–7911.
- (29) Santos, A.; Balderrama, V. S.; Alba, M.; Formentín, P.; Ferré-Borrull, J.; Pallarès, J.; Marsal, L. F. Nanoporous Anodic Alumina Barcodes: Toward Smart Optical Biosensors. *Adv. Mater.* **2012**, *24*, 1050–1054.
- (30) Kumeria, T.; Santos, A.; Rahman, M. M.; Ferré-Borrull, J.; Marsal, L. F.; Losic, D. Advanced Structural Engineering of Nanoporous Photonic Structures: Tailoring Nanopore Architecture to Enhance Sensing Properties. *ACS Photonics* **2014**, *1*, 1298–1306.
- (31) Kumeria, T.; Rahman, M. M.; Santos, A.; Ferré-Borrull, J.; Marsal, L. F.; Losic, D. Structural and Optical Nanoengineering of Nanoporous Anodic Alumina Rugate Filters for Real-Time and Label-Free Biosensing Applications. *Anal. Chem.* **2014**, *86*, 1837–1844.
- (32) Kumeria, T.; Rahman, M. M.; Santos, A.; Ferré-Borrull, J.; Marsal, L. F.; Losic, D. Nanoporous Anodic Alumina Rugate Filters for Sensing of Ionic Mercury: Toward Environmental Point-of-Analysis Systems. *ACS Appl. Mater. Interfaces* **2014**, *6*, 12971–12978.
- (33) Santos, A.; Kumeria, T.; Wang, Y.; Losic, D. In Situ Monitored Engineering of Inverted Nanoporous Anodic Alumina Funnels: On The Precise Generation of 3D Optical Nanostructures. *Nanoscale* **2014**, *6*, 9991–9999.
- (34) Chen, Y.; Santos, A.; Wang, Y.; Kumeria, T.; Wang, C.; Li, J.; Losic, D. Interferometric Nanoporous Anodic Alumina Photonic Coatings for Optical Sensing. *Nanoscale* **2015**, *7*, 7770–7779.
- (35) Kumeria, T.; Santos, A.; Losic, D. Ultrasensitive Nanoporous Interferometric Sensor for Label-Free Detection of Gold(III) Ions. *ACS Appl. Mater. Interfaces* **2013**, *5*, 11783–11790.
- (36) Santos, A.; Kumeria, T.; Losic, D. Nanoporous Anodic Aluminum Oxide for Chemical Sensing and Biosensors. *TrAC, Trends Anal. Chem.* **2013**, *44*, 25–38.
- (37) Santos, A.; Kumeria, T.; Losic, D. Nanoporous Anodic Alumina: A Versatile Platform for Optical Biosensors. *Materials* **2014**, *7*, 4297–4320.
- (38) Kumeria, T.; Santos, A.; Losic, D. Nanoporous Anodic Alumina Platforms: Engineered Surface Chemistry and Structure for Optical Sensing Applications. *Sensors* **2014**, *14*, 11878–11918.
- (39) Liu, Y.; Chang, Y.; Ling, Z.; Hu, X.; Li, Y. Structural Coloring of Aluminum. *Electrochim. Commun.* **2011**, *13*, 1336–1339.
- (40) Yao, Z.; Zheng, M.; Ma, L.; Shen, W. The Fabrication of Ordered Nanoporous Metal Films Based on High Field Anodic Alumina and Their Selected Transmission Enhancement. *Nanotechnology* **2008**, *19*, 465705.
- (41) Yao, Z.; Zheng, M.; Li, H.; Ma, L.; Shen, W. High-Performance Humidity Sensors Based on High-Field Anodized Porous Alumina Films. *Nanotechnology* **2009**, *20*, 395501.
- (42) Wang, Y.; Santos, A.; Evdokiou, A.; Losic, D. Rational Design of Ultra-Short Anodic Alumina Nanotubes by Short-Time Pulse Anodization. *Electrochim. Acta* **2015**, *154*, 379–386.

- (43) Jani, A. M.; Kempson, I. M.; Losic, D.; Voelcker, N. H. Dressing in Layers: Layering Surface Functionalities in Nanoporous Aluminum Oxide Membranes. *Angew. Chem., Int. Ed.* **2010**, *49*, 7933–7937.
- (44) Abràmoff, M. D.; Magalhaes, P. J.; Ram, S. J. Image Processing with ImageJ. *Biophotonics Int.* **2004**, *11*, 36–50.
- (45) Snow, P. A.; Squire, E. K.; Russell, P.; St, J.; Canham, L. T. Vapor Sensing Using The Optical Properties of Porous Silicon Bragg Mirrors. *J. Appl. Phys.* **1999**, *86*, 1781–1784.
- (46) Theiß, W.; Henkel, S.; Arntzen, M. Connecting Microscopic and Macroscopic Properties of Porous Media: Choosing Appropriate Effective Medium Concepts. *Thin Solid Films* **1995**, *255*, 177–180.
- (47) Harper, J.; Sailor, M. J. Detection of Nitric Oxide and Nitrogen Dioxide with Photoluminescent Porous Silicon. *Anal. Chem.* **1996**, *68*, 3713–3717.
- (48) Dronov, R.; Jane, A.; Shapter, J. G.; Hodges, A.; Voelcker, N. H. Nanoporous Alumina-Based Interferometric Transducers Ennobled. *Nanoscale* **2011**, *3*, 3109–3114.
- (49) Orosco, M. M.; Pacholski, C.; Sailor, M. J. Real-Time Monitoring of Enzyme Activity in A Mesoporous Silicon Double Layer. *Nat. Nanotechnol.* **2009**, *4*, 255–258.
- (50) Alvarez, S. D.; Li, C. P.; Chiang, C. E.; Schuller, I. K.; Sailor, M. J. A Label-Free Porous Alumina Interferometric Immunosensor. *ACS Nano* **2009**, *3*, 3301–3307.
- (51) Pacholski, C.; Sartor, M.; Sailor, M. J.; Cunin, F.; Miskelly, G. M. Biosensing Using Porous Silicon Double-Layer Interferometers: Reflective Interferometric Fourier Transform Spectroscopy. *J. Am. Chem. Soc.* **2005**, *127*, 11636–11645.
- (52) Pacholski, C.; Yu, C.; Miskelly, G. M.; Godin, D.; Sailor, M. J. Reflective Interferometric Fourier Transform Spectroscopy: A Self-Compensating Label-Free Immunosensor Using Double-Layers of Porous SiO<sub>2</sub>. *J. Am. Chem. Soc.* **2006**, *128*, 4250–4252.